QUANTUM PHYSICS

A Schrödinger cat living in two boxes

Chen Wang,[1]* Yvonne Y. Gao,[1] Philip Reinhold,[1] R. W. Heeres,[1] Nissim Ofek,[1] Kevin Chou,[1] Christopher Axline,[1] Matthew Reagor,[1] Jacob Blumoff,[1] K. M. Sliwa,[1] L. Frunzio,[1] S. M. Girvin,[1] Liang Jiang,[1] M. Mirrahimi,[1,2] M. H. Devoret,[1] R. J. Schoelkopf[1]*

Quantum superpositions of distinct coherent states in a single-mode harmonic oscillator, known as "cat states," have been an elegant demonstration of Schrödinger's famous cat paradox. Here, we realize a two-mode cat state of electromagnetic fields in two microwave cavities bridged by a superconducting artificial atom, which can also be viewed as an entangled pair of single-cavity cat states. We present full quantum state tomography of this complex cat state over a Hilbert space exceeding 100 dimensions via quantum nondemolition measurements of the joint photon number parity. The ability to manipulate such multicavity quantum states paves the way for logical operations between redundantly encoded qubits for fault-tolerant quantum computation and communication.

Rapid progress in controlling individual quantum systems over the past 20 years (*1*, *2*) has opened a wide range of possibilities of quantum information processing. Potential applications, from universal quantum computation to long-distance quantum communication, share the central theme of exploiting quantum superpositions within a large Hilbert space. Further stimulated by curiosity about the quantum-classical boundary, there has been growing interest in generating superpositions of "macroscopically distinguishable" states that are far apart in phase space. The canonical example is superpositions of coherent states of a harmonic oscillator, i.e. $N(|\alpha\rangle + |-\alpha\rangle)$ with $N \approx 1/\sqrt{2}$ at large $|\alpha|$, known as "cat states." The two components correspond to distinct quasi-classical wave packets, in analogy to Schrödinger's *gedankenexperiment* of an unfortunate cat inside a closed box being simultaneously dead and alive. Cat states have so far been realized with single-mode optical (*3*) or microwave fields (*1*, *4*, *5*) with up to about 100 photons (*6*) but are increasingly susceptible to decoherence at large size.

Manipulating a large number of excitations in such harmonic oscillator states is one of two possible approaches to expand the information capacity of fully controlled quantum systems. Cat states, which span a Hilbert space whose dimension grows linearly with the number of photons, are an attractive approach for redundantly encoding quantum information for error correction (*7*–*9*). The other, more traditional, way to scale up a quantum system is to build many modes of excitations, each operated as a two-level qubit, so that the Hilbert space dimension increases exponentially with the number of modes (*10*, *11*). Is it possible to combine the benefits of both approaches by creating a cat state that lives in more than a single mode or box? The idea of nonlocal or multimode cat dates back to the early days of cavity quantum electrodynamics (QED) (*12*), but experimental demonstration has remained a formidable challenge.

Here, we deterministically create a two-mode cat state of microwave fields in two superconducting cavities, using the strong dispersive interaction with a Josephson junction–based artificial atom. This state can be expressed as

$$|\psi_\pm\rangle = N(|\alpha\rangle_A|\alpha\rangle_B \pm |-\alpha\rangle_A|-\alpha\rangle_B) \qquad (1)$$

where $|\pm\alpha\rangle_A$ and $|\pm\alpha\rangle_B$ are coherent states of two microwave eigenmodes (Alice and Bob) at different frequencies. Each of the two modes is predominantly localized in one of the two cavities that are weakly connected. For convenience, we will refer to the state of each mode as the state of each cavity. Previous realization of the state $|\psi_\pm\rangle$ has been limited to using small and nonorthogonal coherent states (*13*). For larger $|\alpha|$ (i.e., $|\alpha|^2 \gtrsim 2$), $|\psi_\pm\rangle$ can be considered a single cat state living in two boxes, whose superposed components are coherent states in a linearly hybridized mode of Alice and Bob (*14*). Alternatively, in the more natural eigenmode basis, $|\psi_\pm\rangle$ has been known as the entangled coherent states in theoretical studies (*15*) and may also be understood as two single-cavity cat states that are entangled with each other.

The two-mode cat state is an eigenstate of the joint photon number parity operator $\hat{P}_J$.

$$\hat{P}_J = \hat{P}_A\hat{P}_B = e^{i\pi\hat{a}^\dagger\hat{a}}e^{i\pi\hat{b}^\dagger\hat{b}} \qquad (2)$$

where $\hat{a}^\dagger(\hat{a})$ and $\hat{b}^\dagger(\hat{b})$ are the creation (annihilation) operators of photons in Alice and Bob, and $\hat{P}_A$ and $\hat{P}_B$ are the photon number parity operators in individual cavities. Remarkably, $|\psi_+\rangle$ (or $|\psi_-\rangle$) has definitively an even (or odd) number of photons in the two cavities combined, whereas the photon number parity in each cavity separately is maximally uncertain. Quantum nondemolition (QND) measurements of such parity operators not only illustrate the highly nonclassical properties of the state but also are instrumental for quantum error correction in general.

We realize measurements of the joint photon number parity and single-mode parities using the dispersive interaction with three energy levels of an artificial atom. Based on joint parity measurements, we further demonstrate full quantum state tomography of the two-cavity system (*16*). This is obtained in the form of the joint Wigner function $W_J(\beta_A, \beta_B)$, which is a continuous-variable representation of the quantum state with β_A and β_B being complex variables in Alice and Bob, respectively. Without correcting for the infidelity of the $\hat{P}_J$ measurement operator, we observe quantum state fidelity of 81% for a two-mode cat state with $\alpha = 1.92$. The high-quality and high-dimensional quantum control is further manifested by the presence of entanglement exceeding classical bounds in a Clauser-Horne-Shimony-Holt (CHSH)–style inequality for two continuous-variable systems (*16*). Finally, our two-cavity space effectively encodes two coupled logical qubits in the coherent state basis, and we present efficient two-qubit tomography in this encoded space.

Our experiment uses a three-dimensional (3D) circuit QED architecture (*17*), where two high-quality 3D cavities and a quasiplanar readout resonator simultaneously couple to a fixed-frequency transmon-type superconducting artificial atom (Fig. 1, A and B) (*14*). The two cavities that host the cat state of microwave photons are implementations of the longest-lived quantum memory in circuit QED to date (*18*). We use the transmon as an ancilla to manipulate the multiphoton states in the two cavities, and its lowest three levels, $|g\rangle$, $|e\rangle$, and $|f\rangle$, are accessed in this

Table 1. Hamiltonian parameters and coherence times of the two storage cavities and the transmon ancilla. These include transition frequencies ($\omega/2\pi$), energy relaxation times (T_1), Ramsey coherence times (T_2^*), and the dispersive frequency shifts ($\chi/2\pi$) between each cavity and each ancilla transition. The cavity frequencies are given with a precision of ±100 Hz and are stable over the course of several months.

	$\omega/2\pi$	T_1	T_2^*	$\chi^{ge}/2\pi$	$\chi^{ef}/2\pi$
Cavity Alice	4.2196612 GHz	2.2–3.3 ms	0.8–1.1 ms	0.71 MHz	1.54 MHz
Cavity Bob	5.4467679 GHz	1.2–1.7 ms	0.6–0.8 ms	1.41 MHz	0.93 MHz
Ancilla $\|e\rangle\rightarrow\|g\rangle$	4.87805 GHz	65–75 μs	30–45 μs	—	—
Ancilla $\|f\rangle\rightarrow\|e\rangle$	4.76288 GHz	28–32 μs	12–24 μs	—	—

[1]Department of Applied Physics and Physics, Yale University, New Haven, CT 06511, USA. [2]INRIA Paris-Rocquencourt, Domaine de Voluceau, B.P. 105, 78153 Le Chesnay Cedex, France.
*Corresponding author. Email: chen.wang@yale.edu (C.W.); robert.schoelkopf@yale.edu (R.J.S.)

experiment. The device is cooled down to 20 mK in a dilution refrigerator, and microwave transmission through the readout resonator is used to projectively measure the ancilla state with a heterodyne detection at room temperature after multiple stages of amplification.

We consider the Hamiltonian of the system (with parameters listed in Table 1), including two harmonic cavity modes with angular frequencies ω_A and ω_B, a three-level atom with transition frequencies ω_{ge} and ω_{ef}, and their dispersive interaction

$$H/\hbar \approx \omega_A \hat{a}^\dagger\hat{a} + \omega_B \hat{b}^\dagger\hat{b} + \omega_{ge}|e\rangle\langle e| + (\omega_{ge}+\omega_{ef})|f\rangle\langle f|$$
$$-\chi_A^{ge}\hat{a}^\dagger\hat{a}|e\rangle\langle e| - (\chi_A^{ge}+\chi_A^{ef})\hat{a}^\dagger\hat{a}|f\rangle\langle f|$$
$$-\chi_B^{ge}\hat{b}^\dagger\hat{b}|e\rangle\langle e| - (\chi_B^{ge}+\chi_B^{ef})\hat{b}^\dagger\hat{b}|f\rangle\langle f| \quad (3)$$

where χ_i^{ge} and χ_i^{ef} represent the dispersive frequency shifts of cavity i associated with the two ancilla transitions. The readout resonator and small high-order nonlinearities are omitted for simplicity (*14*). Using time-dependent classical drives in the form of microwave pulses, we can perform arbitrary ancilla rotations in both $|g\rangle$–$|e\rangle$ and $|e\rangle$–$|f\rangle$ manifolds and arbitrary cavity state displacements in Alice ($\hat{D}_{\beta_A} = e^{\beta_A\hat{a}^\dagger - \beta_A^*\hat{a}}$) and Bob ($\hat{D}_{\beta_B} = e^{\beta_B\hat{b}^\dagger - \beta_B^*\hat{b}}$) independently. More important, the state-dependent frequency shifts (χ's) allow cavity state manipulations conditioned on the ancilla level or vice versa using spectrally selective control pulses, thus realizing atom-photon quantum logic gates (*6*). It can be further shown that with separate drives on the two cavities and a drive on the ancilla, this Hamiltonian permits universal quantum control of the entire system (*19*).

We generate the two-mode cat state $|\psi_\pm\rangle$ deterministically using a series of logic gates as shown in Fig. 1C (*20*). In particular, we implement effective displacements ($\hat{D}^g_{2\alpha}$) of both cavities conditional on ancilla being in $|g\rangle$ (*14*), which realizes a three-way entangling gate, $\frac{1}{\sqrt{2}}(|g\rangle+|e\rangle)|0\rangle_A|0\rangle_B \rightarrow N(|g\rangle|0\rangle_A|0\rangle_B + |e\rangle|2\alpha\rangle_A|2\alpha\rangle_B)$. Then an ancilla rotation (R_π^{00}) conditional on the cavity state $|0\rangle_A|0\rangle_B$ disentangles the ancilla, and subsequent cavity displacements bring the cavities to a two-mode cat state. The rotation axis determines the sign (or more generally, the phase angle) of the cat state superposition.

We probe the cavity state by QND measurements of the photon number parity. Parity measurement of a single cavity has been previously demonstrated (*9*, *21*), where a conditional cavity phase shift (*4*), $C_\phi = \mathbf{I}\otimes|g\rangle\langle g| + e^{i\phi\hat{a}^\dagger\hat{a}}\otimes|e\rangle\langle e|$, with $\phi = \pi$, maps cavity states with even or odd photon numbers to $|g\rangle$ or $|e\rangle$ of a two-level ancilla, respectively, for subsequent readout. To achieve joint parity mapping in our two-cavity system, we exploit three levels of the ancilla to realize simultaneous C_π in both Alice and Bob. With the ancilla frequency designed to be in between those of the two cavities, the $|e\rangle\rightarrow|g\rangle$ transition shows stronger interaction with Bob ($\chi_B^{ge} > \chi_A^{ge}$), whereas the $|f\rangle\rightarrow|e\rangle$ transition shows stronger interaction with Alice ($\chi_A^{ef} > \chi_B^{ef}$). Manipulating the ancilla in different superposition states among the three levels allows us to concatenate conditional phase gates associated with χ_i^{ge} and χ_i^{ef} with arbitrary weights (*14*). This additional degree of freedom not only allows for measurement of $\hat{P}_J$ but also enables parity measurement of each cavity individually without affecting the other.

Based on single-cavity parity measurements, we can measure the Wigner function of individual cavities, $W_i(\beta_i) = \frac{2}{\pi}\mathrm{Tr}[\rho\hat{D}_{\beta_i}\hat{P}_i\hat{D}^\dagger_{\beta_i}]$ ($i = A$ or B) (*5*, *21*). The Wigner function is a standard method to fully determine the quantum state of a single-continuous-variable system, which represents the quasiprobability distribution of photons in the quadrature space [Re(β)-Im(β)]. Our measured W_A and W_B for a two-mode cat state $|\psi_-\rangle$ with α = 1.92 (Fig. 2) illustrates that the quantum state of either Alice or Bob on its own is a statistical mixture of two clearly separated coherent states. However, single-cavity Wigner functions do not contain full information on the global quantum state. We find strong correlation between cavities by measuring joint photon number party $\langle\hat{P}_J\rangle = -0.81\pm0.01$, even though each cavity alone shows mean photon number parity of $\langle\hat{P}_A\rangle \approx \langle\hat{P}_B\rangle \approx 0$. Additional evidence of the joint parity can be seen in a spectroscopy measurement (*14*).

A full quantum state tomography of the two-cavity system can be realized by measuring the joint Wigner function (*22*):

$$W_J(\beta_A,\beta_B) = \frac{4}{\pi^2}\mathrm{Tr}[\rho\hat{D}_{\beta_A}\hat{D}_{\beta_B}\hat{P}_J\hat{D}_{\beta_B}\hat{D}^\dagger_{\beta_A}]$$
$$\equiv \frac{4}{\pi^2}P_J(\beta_A,\beta_B) \quad (4)$$

W_J is a function in the 4D phase space, whose value at each point [Re(β_A), Im(β_A), Re(β_B), and Im(β_B)], after rescaling by $\pi^2/4$, can be directly measured from the expectation value of the joint parity after independent displacements in Alice and Bob (*16*). We will therefore use the scaled joint Wigner function, or "displaced joint parity function," $P_J(\beta_A,\beta_B)$ to represent the cavity state. To illustrate the core features in this 4D Wigner function of the state $|\psi_-\rangle$, we show its 2D cuts along the Re(β_A)-Re(β_B) plane and Im(β_A)-Im(β_B) plane for both the calculated ideal state (Fig. 3, A

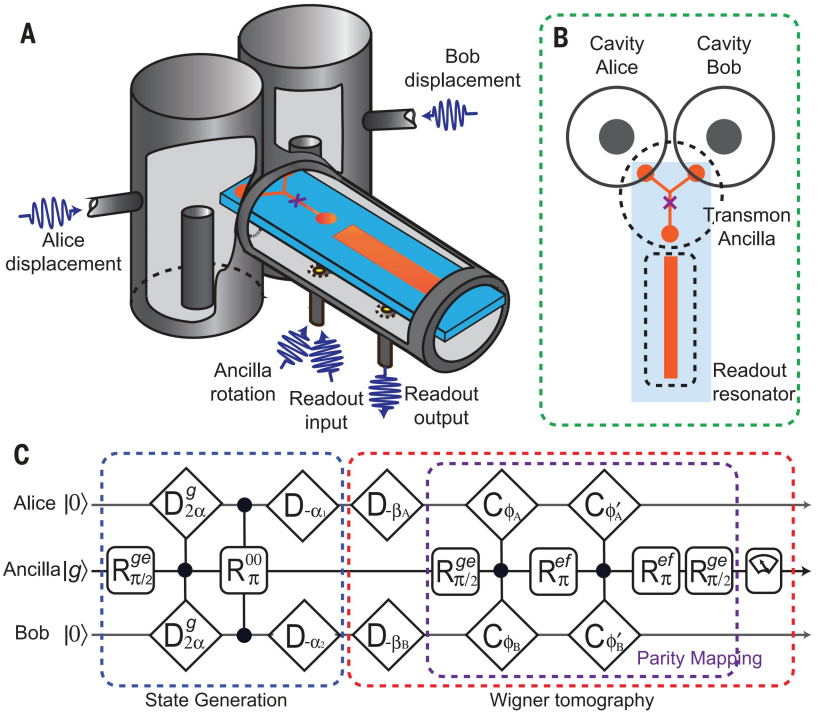

Fig. 1. Cartoon schematic of device architecture and experimental protocol. (**A**) A 3D view of the device consisting of two coaxial cavities (Alice and Bob), a Y-shaped transmon with a single Josephson junction (marked by ×), and a stripline readout resonator. All components are housed inside a single piece of bulk high-purity aluminum, with artificial windows drawn for illustration purposes. (**B**) A top view of the same device, showing the relative position of the sapphire chip, center posts of the coaxial cavities, transmon antenna, and the readout resonator. (**C**) The microwave control sequences for generating the two-mode cat state and performing Wigner tomography. $\hat{D}_\beta$ represents cavity displacement by β, and a superscript *g* is added if the displacement is conditional on the ancilla being in $|g\rangle$. R_θ^{ge} or R_θ^{ef} represents ancilla rotation by θ (around an axis in the *x*-*y* plane) in the $|g\rangle$–$|e\rangle$ or $|e\rangle$–$|f\rangle$ manifold. R_π^{00} is an ancilla $|g\rangle$–$|e\rangle$ rotation conditional on the cavities being in $|0\rangle_A|0\rangle_B$. $C_\phi$represents a cavity phase shift of ϕ, conditional on the ancilla being in an excited state. By choosing $\phi_i + \phi_i' = \pi$ or 2π, we can measure photon number parity of Alice ($\hat{P}_A$), Bob ($\hat{P}_B$), or the two combined ($\hat{P}_J$), to perform Wigner tomography of individual cavities or the joint Wigner tomography.

and B) (*16*) and the measured data (Fig. 3, C and D). The Wigner function contains two positively valued Gaussian hyperspheres representing the probability distribution of the two coherent-state components and an interference structure around the origin with strong negativity. Excellent agreement is achieved between measurement and theory, with the raw data showing an overall 81% contrast of the ideal Wigner function. Comprehensive 4D measurements of P_J further allow us to reconstruct the density matrix of the quantum state, which shows a total fidelity of also about 81% against the ideal $|\psi_-\rangle$ state. The actual state fidelity may be substantially higher if various errors associated with tomography are removed (*14*). Additional visualization of the Wigner function data is presented in a supplementary movie (*14*).

Analyzed within the eigenmode basis, the two-mode cat state is a manifestation of quantum entanglement between two quasiclassical systems. The entanglement can be tested against a CHSH-style Bell's inequality constructed from P_J at four points in the phase space (*16*). We observe a Bell signal (*14*) of 2.17 ± 0.01 for the state in Fig. 3, exceeding the classical bound of 2. Without complete spatial separation and fully independent readout of the two modes, this violation should be considered a demonstration of the fidelity of the entanglement and the measurement rather than a true test of nonlocality. Nevertheless, various schemes exist to further separate the two modes, such as converting the cavity fields into itinerant microwave signals and/or optical photons (*23*).

Compared with other experimentally realized quantum states of two harmonic oscillators, a striking property of the two-mode cat state is that its underlying compositions are highly distinguishable. Two-mode squeezed states in various physical implementations—e.g. (*24*)—show strong entanglement but are Gaussian states without the Wigner negativity and the phase space separation, as in a cat state. Generation of the "*N*00*N*" state, an entangled state in the discrete Fock state basis, typically requires quantum

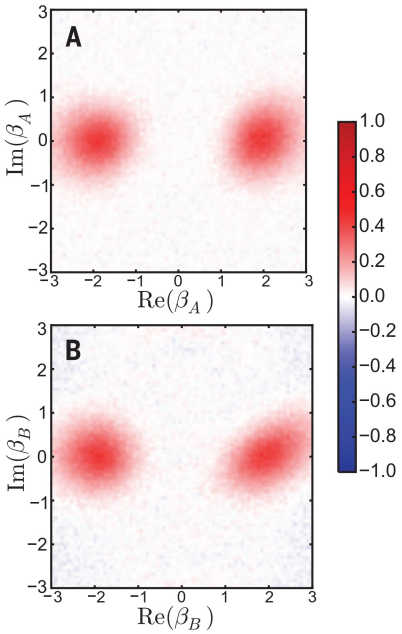

Fig. 2. Wigner tomography of individual cavities. Measured scaled Wigner function of (**A**) Alice $[\frac{\pi}{2}W_A(\beta_A)]$ and (**B**) Bob $[\frac{\pi}{2}W_B(\beta_B)]$, respectively, for the two-mode cats state $|\psi_-\rangle$, each plotted in the complex plane of Re(β_i) and Im(β_i) (i = A or B). For either cavity, the lack of interference fringes indicates a statistical mixture of two coherent states, in striking contrast to the regular (single-mode) cat state that can also be straightforwardly generated in our experiment (*14*). The distortion of the coherent states is due to higher-order Hamiltonian terms (*14*). The photon number parity within each cavity is close to 0, reflected by the value of respective Wigner functions near the origin.

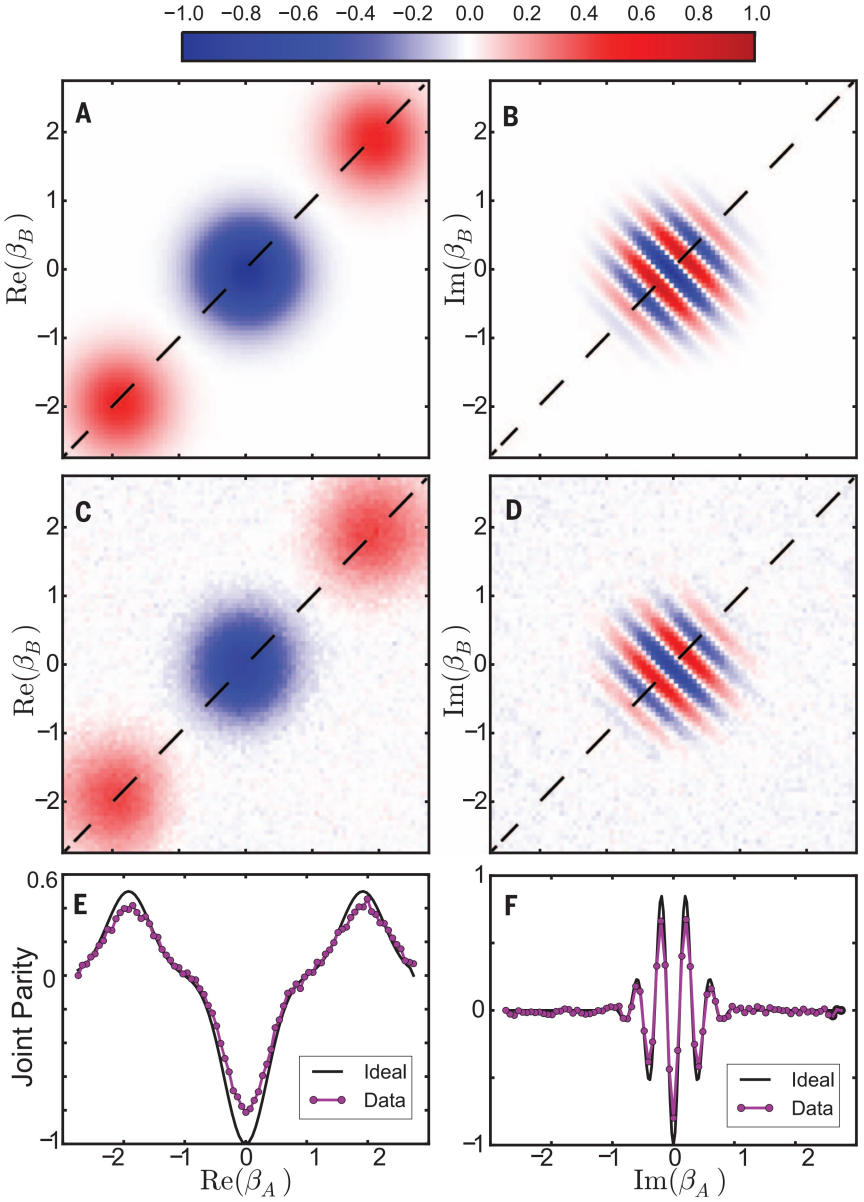

Fig. 3. Joint Wigner tomography. (**A** and **B**) A 2D plane-cut along (A) axes Re(β_A)-Re(β_B) and (B) axes Im(β_A)-Im(β_B) of the calculated 4D scaled joint Wigner function $P_J(\beta_A, \beta_B)$ of the ideal odd-parity two-mode cat state $|\psi_-\rangle$ with $\alpha = 1.92$. The red features in (A) represent the probability distribution of the two coherent states components. The central blue feature in (A) and fringes in (B) demonstrate quantum interference between the two components. (**C** and **D**) The corresponding Re(β_A)-Re(β_B) and Im(β_A)-Im(β_B) plane-cuts of the measured $P_J(\beta_A, \beta_B)$ of $|\psi_-\rangle$, to be compared with the ideal results in (A) and (B), respectively. Data are taken in an 81 by 81 grid, where every point represents an average of about 2000 binary outcomes of joint parity measurements. (**E**) Diagonal line-cuts of the data shown in (A) and (C), corresponding to 1D plots of the calculated (black) and measured (purple) scaled joint Wigner function along Re(β_A) = Re(β_B) with Im(β_A) = Im(β_B) = 0. (**F**) Diagonal line-cuts of the data shown in (B) and (D), corresponding to 1D plots of the calculated (black) and measured (purple) scaled joint Wigner function along Im(β_A) = Im(β_B), with Re(β_A) = Re(β_B) = 0.

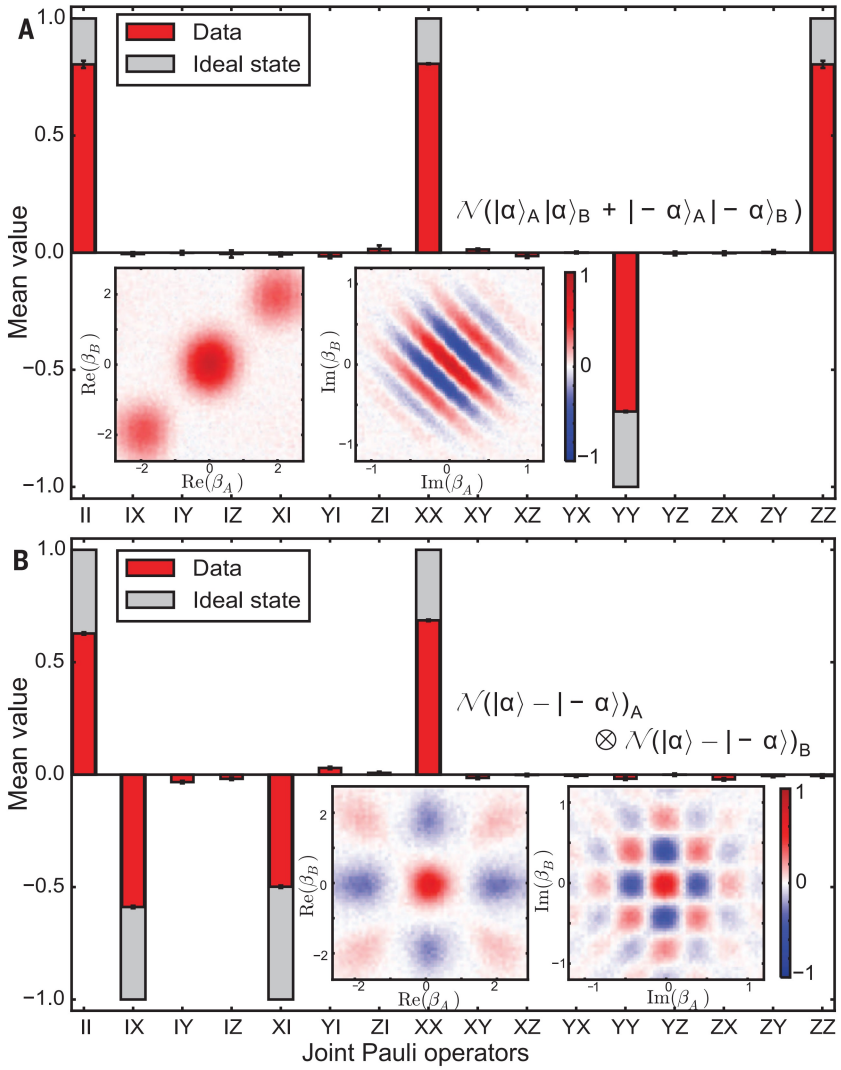

Fig. 4. Encoded two-qubit tomography. (**A**) Red bars show tomography of two logical qubits encoded in the coherent state basis of two cavities, with the prepared state being an even-parity two-mode cat state, $|\psi_+\rangle$ with $\alpha = 1.92$. Gray bars represent the ideal state. Insets show the Re(β_A)-Re(β_B) and Im(β_A)-Im(β_B) plane-cuts of the measured scaled joint Wigner function of the same state. (**B**) Encoded two-qubit tomography of an approximate product state of single-cavity cat states, $N(|\alpha\rangle_A - |-\alpha\rangle_A) \otimes N(|\alpha\rangle_B - |-\alpha\rangle_B)$, also with $\alpha = 1.92$. Insets show plane-cuts of the measured P_J of the same state. These Wigner function patterns can be understood by considering $W_J(\beta_A, \beta_B) = W_A(\beta_A)W_B(\beta_B)$ for separable states. For example, the checkerboard patterns in the Im(β_A)-Im(β_B) plane-cuts arise from multiplying orthogonal fringes from the two independent cat states.

operations of photons one by one and so far has been limited to five photons (*25*, *26*). The two components of the cat state shown here are separated by a distance of $\sqrt{30}$ in the 4D phase space, giving a cat size (*5*) of 30 photons. Our technique in principle allows generation of two-mode cat states with arbitrary size. So far, we have measured cat sizes of up to 80 photons (*14*), and more macroscopic states can be achieved by implementing numerically optimized control pulses.

Compared with single-cavity quantum states, the addition of the second cavity mode increases the quantum information capacity significantly. Despite the modest mean photon numbers, a full tomography of the two-mode cat state (partly shown in Fig. 3) requires a Hilbert space of at least 100 dimensions to be described (capturing 99% of the population), comparable to a six- or seven-qubit Greenberger-Horne-Zeilinger (GHZ) state. Our conservatively estimated quantum state fidelity is comparable to that reported for an eight-qubit GHZ state in trapped ions (*10*) and the largest GHZ state in superconducting circuits (five qubits) (*11*).

An important motivation for creating multicavity cat states is to implement a promising paradigm toward fault-tolerant quantum computation (*7*, *8*), where information is redundantly encoded in the quasi-orthogonal coherent state basis (*6*). This approach has recently led to the first realization of quantum error correction of a logical qubit achieving the break-even point (*9*). In this context, our experiment realizes an architecture of two coupled logical qubits, where the coherent states $|\pm\alpha\rangle$ in each of the two cavities represent $|0\rangle$ and $|1\rangle$ of a logical qubit. For any two-qubit logical state encoded in this subspace, we can perform efficient tomography without extensive measurement of the joint Wigner function. This is carried out by measuring $P_J(\beta_A, \beta_B)$ at 16 selected points (*14*). The encoded two-qubit tomography of a state $|\psi_+\rangle$ with $\alpha = 1.92$ is shown in Fig. 4A, providing a direct fidelity estimation (*27*) of $\frac{1}{4}(\langle\hat{I}\hat{I}\rangle + \langle\hat{X}\hat{X}\rangle - \langle\hat{Y}\hat{Y}\rangle + \langle\hat{Z}\hat{Z}\rangle) = 78\%$ against the ideal Bell state, surpassing the 50% bound for classical correlation. As a comparison, Fig. 4B illustrates a product state of single-mode cat states in Alice and Bob, equivalent to $|-X\rangle_A|-X\rangle_B$ in the logical space. For both states illustrated here, the two-qubit tomography suggests that errors within the encoded space are quite small. The reduced overall contrast, as indicated by the measured identity operator smaller than 1, can be attributed to the infidelity of the joint parity measurement and leakage from the code space (due to higher-order Hamiltonian terms).

We have demonstrated a Schrödinger's cat that lives in two cavities. This two-mode cat state is not only a manifestation of mesoscopic superposition and entanglement constructed from quasiclassical states (*15*) but also a resource for quantum metrology (*28*), quantum networks, and teleportation (*29*). Moreover, the demonstration of high-fidelity quantum control over the large two-cavity Hilbert space has important implications for continuous-variable-based quantum computation. The measurement of the joint photon number parity realized here is QND by design and will play a central role in quantum error correction (*7*, *9*, *19*) and facilitating concurrent remote entanglement (*30*) in a modular architecture of quantum computation.

REFERENCES AND NOTES

1. S. Haroche, *Rev. Mod. Phys.* **85**, 1083–1102 (2013).
2. D. J. Wineland, *Rev. Mod. Phys.* **85**, 1103–1114 (2013).
3. A. Ourjoumtsev, H. Jeong, R. Tualle-Brouri, P. Grangier, *Nature* **448**, 784–786 (2007).
4. M. Brune *et al.*, *Phys. Rev. Lett.* **77**, 4887–4890 (1996).
5. S. Deléglise *et al.*, *Nature* **455**, 510–514 (2008).
6. B. Vlastakis *et al.*, *Science* **342**, 607–610 (2013).
7. I. L. Chuang, D. W. Leung, Y. Yamamoto, *Phys. Rev. A* **56**, 1114–1125 (1997).
8. M. Mirrahimi *et al.*, *New J. Phys.* **16**, 045014 (2014).
9. N. Ofek, *et al.*, Quantum error correction that extends the lifetime of quantum information. http://arxiv.org/abs/1602.04768 (2016).
10. T. Monz *et al.*, *Phys. Rev. Lett.* **106**, 130506 (2011).
11. J. Kelly *et al.*, *Nature* **519**, 66–69 (2015).
12. L. Davidovich, A. Maali, M. Brune, J. M. Raimond, S. Haroche, *Phys. Rev. Lett.* **71**, 2360–2363 (1993).
13. A. Ourjoumtsev, F. Ferreyrol, R. Tualle-Brouri, P. Grangier, *Nat. Phys.* **5**, 189–192 (2009).
14. For additional information, see the supplementary materials on *Science* Online.
15. B. C. Sanders, *J. Phys. A: Math. Theor.* **45**, 244002 (2012).
16. P. Milman *et al.*, *Eur. Phys. J. D* **32**, 233–239 (2005).
17. H. Paik *et al.*, *Phys. Rev. Lett.* **107**, 240501 (2011).

18. M. Reagor *et al.*, A quantum memory with near-millisecond coherence in circuit QED. http://arxiv.org/abs/1508.05882 (2015).
19. M. H. Michael *et al.*, New class of quantum error-correcting codes for a bosonic mode. http://arxiv.org/abs/1602.00008 (2016).
20. Z. Leghtas *et al.*, *Phys. Rev. A* **87**, 042315 (2013).
21. P. Bertet *et al.*, *Phys. Rev. Lett.* **89**, 200402 (2002).
22. K. E. Cahill, R. J. Glauber, *Phys. Rev.* **177**, 1882–1902 (1969).
23. R. W. Andrews *et al.*, *Nat. Phys.* **10**, 321–326 (2014).
24. Z. Y. Ou, S. F. Pereira, H. J. Kimble, K. C. Peng, *Phys. Rev. Lett.* **68**, 3663–3666 (1992).
25. I. Afek, O. Ambar, Y. Silberberg, *Science* **328**, 879–881 (2010).
26. H. Wang *et al.*, *Phys. Rev. Lett.* **106**, 060401 (2011).
27. S. T. Flammia, Y.-K. Liu, *Phys. Rev. Lett.* **106**, 230501 (2011).
28. J. Joo, W. J. Munro, T. P. Spiller, *Phys. Rev. Lett.* **107**, 083601 (2011).
29. S. J. van Enk, O. Hirota, *Phys. Rev. A* **64**, 022313 (2001).
30. A. Roy, L. Jiang, A. D. Stone, M. Devoret, *Phys. Rev. Lett.* **115**, 150503 (2015).

ACKNOWLEDGMENTS

We thank A. Petrenko, Z. Leghtas, B. Vlastakis, W. Pfaff, M. Silveri, R. T. Brierley, and A. Roy for helpful discussions, and M. J. Hatridge and A. Narla for assistance on the parametric amplifier. This research was supported by the U.S. Army Research Office (W911NF-14-1-0011), NSF DMR-1301798, and the Multidisciplinary University Research Initiatives program (MURI) through the Air Force Office of Scientific Research (FA9550-14-1-0052). Facilities use was supported by the Yale Institute for Nanoscience and Quantum Engineering (YINQE), the Yale SEAS cleanroom, and the NSF (MRSECDMR 1119826). Y.Y.G. acknowledges support from a National Science Scholarship from Agency for Science, Technology, and Research (A*STAR) of Singapore.

SUPPLEMENTARY MATERIALS

www.sciencemag.org/content/352/6289/1087/suppl/DC1
Materials and Methods
Supplementary Text
Figs. S1 to S16
Tables S1 to S3
Movie S1
References (*31*–*49*)

20 January 2016; accepted 14 April 2016
10.1126/science.aaf2941

QUANTUM SIMULATION

Experimental reconstruction of the Berry curvature in a Floquet Bloch band

N. Fläschner,[1,2]* B. S. Rem,[1,2]* M. Tarnowski,[1] D. Vogel,[1] D.-S. Lühmann,[1] K. Sengstock,[1,2,3]† C. Weitenberg[1,2]

Topological properties lie at the heart of many fascinating phenomena in solid-state systems such as quantum Hall systems or Chern insulators. The topology of the bands can be captured by the distribution of Berry curvature, which describes the geometry of the eigenstates across the Brillouin zone. Using fermionic ultracold atoms in a hexagonal optical lattice, we engineered the Berry curvature of the Bloch bands using resonant driving and show a full momentum-resolved measurement of the ensuing Berry curvature. Our results pave the way to explore intriguing phases of matter with interactions in topological band structures.

Topology is a fundamental concept for our understanding of many fascinating systems, such as topological superconductors or topological insulators, which conduct only at their edges (*1*). The topology of the bulk band is quantified by the Berry curvature (*2*), the integral of which over the full Brillouin zone is a topological invariant called the Chern number. According to the bulk boundary correspondence principle, the Chern number determines the number of chiral conducting edge states (*1*). Although edge states have been directly observed in a variety of lattice systems—ranging from solid-state systems to photonic waveguides, and even coupled mechanical pendula (*3*–*7*)—the underlying Berry curvature as the central measure of topology is not easily accessible. In recent years, ultracold atoms in optical lattices have emerged as a platform with which to study topological band structures (*8*, *9*), and these systems have seen considerable experimental and theoretical progress. Whereas in condensed-matter systems, topological properties arise thanks to external magnetic fields or intrinsic spin-orbit coupling of the material, in cold atom systems they can be engineered by periodic driving analogous to illuminated graphene (*10*, *11*). The resulting Floquet system can have topological properties very different from those of the original system (*12*). The driving can, for example, be realized through lattice shaking (*13*–*17*) or Raman coupling (*18*–*20*) with high-precision control in a large parameter space. In particular, the driving can break time-reversal symmetry (*14*, *15*, *17*) and thus allows for engineering nontrivial topology (*17*, *19*). In quantum gas experiments, topological properties have been probed via the Hall drift of accelerated wave packets (*17*, *19*), via an interferometer in momentum space (*21*, *22*), and via edge states (*23*, *24*), but so far, the full underlying Berry curvature was not measured quantitatively.

We measured the Berry curvature with full momentum resolution based on a method proposed in (*25*, *26*). We performed a full tomography of the Bloch states across the entire Brillouin zone by observing the dynamics at each momentum point after a projection onto flat bands. The topological bands were engineered through resonant dressing of the two lowest bands of an artificial boron nitride lattice and feature a rich distribution of Berry curvature. Other relevant quantities such as the Berry phase or the Chern number can easily be obtained from the Berry curvature, which is thus the central concept for the description of topology.

Our system consists of ultracold fermionic atoms in a hexagonal optical lattice (*27*) formed by three interfering laser beams. With an appropriate polarization (*28*), a variable energy offset $h\Delta_{AB}$ between the A and B sites (Fig. 1A), which breaks inversion symmetry, can be engineered. With the emerging band gap hv_{AB}, the Dirac points at K and K′ become massive, and for a large offset, the bands are flat (Fig. 1B) (*28*). This is a key ingredient for our tomography, because the flat band acts as the reference frame in which we reconstruct the eigen states. Then as a central experimental method, we could accelerate the lattice on circular trajectories in real space by modulating the phases of the three lattice beams, thus realizing circular shaking (*13*–*17*). When the shaking frequency is near resonant with respect to a band transition, the two bands couple and form two new dressed Floquet bands. In Fig. 1C, we show the dressed Floquet bands for different accessible driving amplitudes. Apart from the dramatic change in the dispersion relation, the topological properties of the bands are changed. This manifests itself in the creation of a new Dirac point at the Γ-point and the annihilation of a Dirac point at the K point (Fig. 1D). A threefold symmetry also becomes visible in the dispersion relation (Fig. 1E).

The topological properties are not captured by the mere dispersion relation but by the Berry curvature, which describes the winding of the eigenstates across the Brillouin zone. Therefore, a complete tomography of the eigenstates of a Bloch band is mandatory for a measurement of the Berry curvature. The key idea behind our tomography is to reconstruct the eigenvectors from dynamics after a projection onto flat bands (*26*). Consider the Bloch sphere (Fig. 2A), whose poles are given by $|\mathbf{k},A\rangle$ and $|\mathbf{k},B\rangle$, which are the Bloch states restricted to the A and B sublattice, respectively. The lower band can be written as $|\mathbf{k}\rangle = \sin(\theta_k/2)|\mathbf{k},A\rangle - \cos(\theta_k/2)\exp(i\phi_k)|\mathbf{k},B\rangle$, and after a projection onto flat bands, the state oscillates around $|\mathbf{k},B\rangle$, with the frequency v_k

[1]Institut für Laserphysik (ILP), Universität Hamburg, Luruper Chaussee 149, 22761 Hamburg, Germany. [2]Hamburg Centre for Ultrafast Imaging, Luruper Chaussee 149, 22761 Hamburg, Germany. [3]Zentrum für Optische Quantentechnologien (ZOQ), Universität Hamburg, Luruper Chaussee 149, 22761 Hamburg, Germany.
*These authors contributed equally to this work. †Corresponding author. Email: klaus.sengstock@physnet.uni-hamburg.de